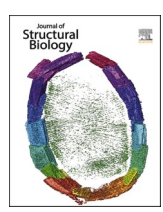
ELSEVIER

Contents lists available at ScienceDirect

Journal of Structural Biology

journal homepage: www.elsevier.com/locate/yjsbi



Research Article



Matrix/mineral ratio and domain size variation with bone tissue age: A photothermal infrared study

Taeyong Ahn ^a, Max Jueckstock ^b, Gurjit S. Mandair ^c, James Henderson ^f, Benjamin P. Sinder ^d, Kenneth M. Kozloff ^{d,e,*}, Mark M. Banaszak Holl ^{g,*}

- ^a Macromolecular Science and Engineering, University of Michigan, Ann Arbor, MI, USA
- b Department of Chemistry, University of Michigan, Ann Arbor, MI, USA
- Dentistry, University of Michigan, Ann Arbor, MI, USA
- ^d Orthopaedic Surgery, University of Michigan, Ann Arbor, MI, USA
- e Biomedical Engineering, University of Michigan, Ann Arbor, MI, USA
- f Center for Statistical Consultation and Research (CSCAR), University of Michigan, Ann Arbor, MI, USA
- ^g Chemical and Biological Engineering, Monash University, Melbourne, Victoria, Australia

ARTICLE INFO

Edited by Andreas H Engel

Keywords:
Bone
Mineralized collagen fibril
Nanoscale chemical heterogeneity
AFM-IR
O-PTIR
Mineralization domain size
Matrix/mineral ratio

ABSTRACT

Atomic force microscopy-infrared spectroscopy (AFM-IR) and optical photothermal infrared spectroscopy (O-PTIR), which feature spectroscopic imaging spatial resolution down to ~ 50 nm and ~ 500 nm, respectively, were employed to characterize the nano- to microscale chemical compositional changes in bone. Since these changes are known to be age dependent, fluorescently labelled bone samples were employed. The average matrix/mineral ratio values decrease as the bone tissue matures as measured by both AFM-IR and O-PTIR, which agrees with previously published FTIR and Raman spectroscopy results. IR ratio maps obtained by AFM-IR reveal variation in matrix/mineral ratio-generating micron-scale bands running parallel to the bone surface as well as smaller domains within these bands ranging from ~ 50 to 700 nm in size, which is consistent with the previously published length scale of nanomechanical heterogeneity. The matrix/mineral changes do not exhibit a smooth gradient with tissue age. Rather, the matrix/mineral transition occurs sharply within the length scale of 100-200 nm. O-PTIR also reveals matrix/mineral band domains running parallel to the bone surface, resulting in waves of matrix/mineral ratios progressing from the youngest to most mature tissue. Both AFM-IR and O-PTIR show a greater variation in matrix/mineral ratio value for younger tissue as compared to older tissue. Together, this data confirms O-PTIR and AFM-IR as techniques that visualize bulk spectroscopic data consistent with higher-order imaging techniques such as Raman and FTIR, while revealing novel insight into how mineralization patterns vary as bone tissue ages.

1. Introduction

Vibrational spectroscopy techniques such as Fourier-transform infrared spectroscopy (FTIR) (Boskey and Pleshko Camacho, 2007; Lopes et al., 2018; Paschalis et al., 2011) and Raman spectroscopy (Morris and Mandair, 2011) have been extensively utilized to study chemical composition in bone and other biological tissues such as cartilage, enamel and dentin. However, the practical spatial resolution determined by both energy wavelength and limitations of available optics for many literature FTIR microscopy studies (\sim 10 μ m) (Miller and Smith, 2005) and literature Raman spectroscopy studies (\sim 2 to 5 μ m)

(De Carmejane et al., 2005; Gamsjaeger et al., 2010; Gong et al., 2013; Nyman et al., 2011), prevented examining chemical variation below the resolution of the bone lamellae structure (Fig. 1). These limitations are prompting studies with improved resolution by Raman imaging (\sim 0.5–1.0 μ m) and FTIR imaging (\sim 1 μ m). In addition to the inherent spatial resolution limit, bone samples probed by conventional transmission infrared microscopy need to be chemically dehydrated and sliced into micron thick sections for measurement purposes. Raman spectroscopy, which can be employed for surface-based imaging on fully hydrated samples, has an inherently lower signal to noise ratio than FTIR as the Raman effect is quite weak (typically, 1 in 108 of the incident

E-mail address: mark.banaszakholl@monash.edu (M.M. Banaszak Holl).

^{*} Corresponding authors at: Orthopaedic Surgery, University of Michigan, Ann Arbor, MI, USA (K.M. Kozloff). Department of Chemical & Biological Engineering, Monash University, Clayton, Victoria 3800, Australia (M.M. Banaszak Holl).

photons undergo Raman scattering) (Morris and Mandair, 2011; Jones et al., 2019; Taylor and Donnelly, 2020).

Atomic force microscopy-infrared spectroscopy (AFM-IR) is a novel infrared spectroscopy technique that utilizes an AFM tip as a probing method (Fig. 1A) to achieve a nominal spatial resolution of ~ 50 nm (contact mode) (Dazzi et al., 2012; Dazzi and Prater, 2017). Optical photothermal infrared spectroscopy (O-PTIR) is another newly developed infrared characterization technique that employs a green laser (wavelength of 532 nm) as a probing method (Fig. 1B) to achieve a ~ 0.5 to 1 μm spatial resolution (Kansiz et al., 2020). Both AFM-IR and O-PTIR can aquire chemical information on fully hydrated thick bone samples.

AFM-based nanoindentation studies demonstrate that bone has nanoscale mechanical heterogeneity with a length scale of one or two collagen fibrils (diameter ~ 20 to 250 nm) (Tai et al., 2007; Yao et al., 2011). These studies suggest that mechanical heterogeneity at the nanoscale may enhance energy dissipation in bone, thus sparking an interest in better understanding the variation in chemical composition at these length scales. A few studies have employed AFM-IR to study biological tissues such as bone (Gourion-Arsiguaud et al., 2014; Imbert et al., 2018), dentin (Huang et al., 2020; Sereda et al., 2019), and anterior cruciate ligament (Chen et al., 2019). In particular, Imbert et al. validated the AFM-IR method by comparing spectra of the same poly (methylmethacrylate) (PMMA) and bone samples measured by AFM-IR and FTIR. For ovine cancellous bone, they showed increasing mineralization with tissue maturity (Imbert et al., 2018). To date, there is no bone study utilizing O-PTIR; however, various scientific fields have adopted O-PTIR to characterize atmospheric particles (Olson et al., 2020), Alzheimer's disease-related amyloid protein aggregation in neurons (Klementieva et al., 2020), pharmaceutical dry powder aerosols (Khanal et al., 2020), and polarization-dependent spectral changes in a single collagen-fibril (Bakir et al., 2020).

The purpose of this study was to evaluate the age-dependent changes in matrix/mineral ratio in mouse femur bone tissue by employing complementary AFM-IR and O-PTIR methods in two different regions of interest from rapidly growing (2-month-old) and adult (7-month-old) mice. Due to the growth rate difference between the two sets of mice, the rapidly growing 2-month-old mice have a ~ 6 times larger cross-sectional area of bone up to the 5 weeks-old tissue age as compared to the adult mice, whose new bone periosteal apposition has largely ceased. Although AFM-IR provides an order of magnitude higher spatial

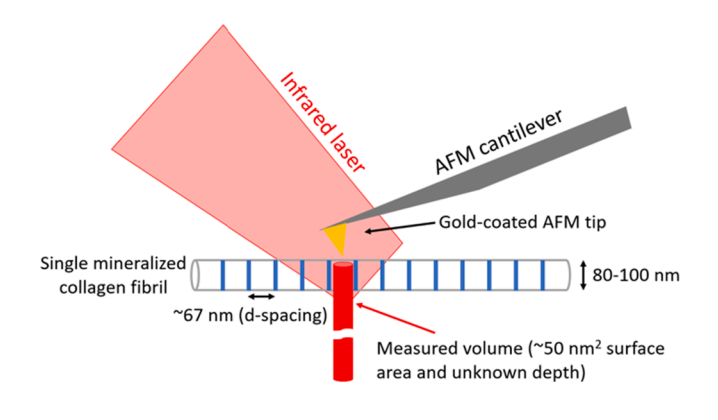
resolution than O-PTIR, the slower scanning of the AFM cantilever greatly increases data collection time, particularly for creating hyperspectral chemical maps. O-PTIR, which is a purely optical technique, is more suitable for collecting hyperspectral chemical information from large region of interests due to its order of magnitude quicker data acquisition time. Both rapidly growing (2-month-old) and adult (7month-old) mice were employed with each sample set containing multiple fluorescence markers to provide a rigorous control of tissue age. In order to further validate photothermal infrared analysis of bone, the AFM-IR and O-PTIR methods are compared to each other as well as to high-resolution Raman microscopy. This study adds new data, including micron-scale infrared maps, characterizing the changes in matrix/mineral as a function of age and highlights multiple changes occurring on the 0.1-5.0 µm scale including range of domain sizes (~50-700 nm), change in extent of variation of matrix/mineral with age, a comparison to previously reported nanomechanical domains, and the relationship of the micron scale matrix/mineral bands with the age-dependent fluorescent staining that were not resolvable in previous high-resolution FTIR and Raman microscopy studies.

2. Materials and methods

2.1. Sample preparation

Nine male wild type mouse femur samples (five 7-month-old adults and four 2-month-old rapidly growing juveniles at death) were prepared from samples described by Sinder et al. (Sinder et al., 2016), including the fluorescence injection scheme (labeled for day 1, week 1, week 3 and week 5 tissue ages), polymer encasing, and sectioning. For AFM-IR and O-PTIR analysis, two more steps were required. First, since the original samples were too thick for both instruments, the samples were sectioned to 4 to 5 mm thickness by a low-speed rotary saw (IsoMet; Buehler, Lake Bluff, Illinois, USA). Second, polishing steps with P1200, P2400, P4000 and 3 μ m diamond suspension (Buehler, Lake Bluff, Illinois, USA) were performed for 10 s per step. After polishing, the samples were washed with distilled water. To give a point of reference for the different measurement techniques, a fiducial mark was cut with a sharp knife onto the bone surface.

A) AFM-IR



B) O-PTIR

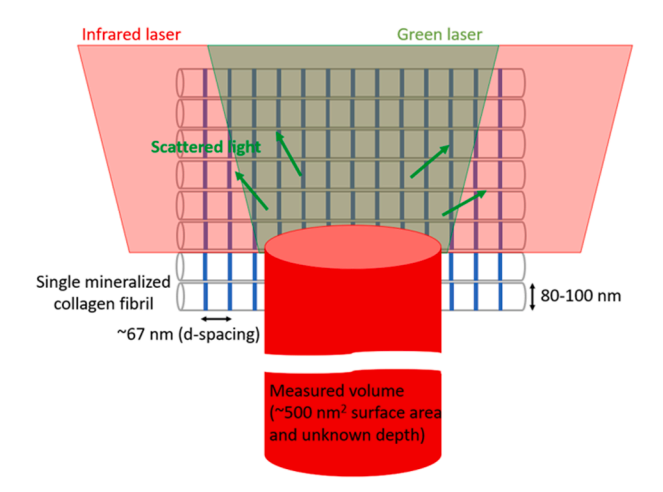


Fig. 1. Spectroscopic sampling volumes for A) AFM-IR and B) O-PTIR with respect to the size of mineralized collagen fibrils in bone. The area of the red cylinder cap indicates the approximate surface area from which individual infrared spectrum is obtained. The depth of the cylinder indicates the sampling depth of each technique, which is an unknown distance dependent on laser power and material properties such as the thermal transport coefficient. (For interpretation of the references to color in this figure legend, the reader is referred to the web version of this article.)

2.2. Fluorescence imaging

An upright Nikon microscope with a DS-Fi2 digital camera (Nikon Eclipse Ni-U, Tokyo, Japan) was employed to take calcein and alizarin fluorescence images with a 10X dry objective. Since the fluorescence signal from the alizarin dye was typically weaker than that of the calcein dye, the exposure time for the alizarin image was adjusted to match the fluorescence signal intensity of the calcein image. NIS BR software (Nikon, Champigny-sur-Marne, France) was used to combine both calcein and alizarin images with a scale bar (Fig. 2B). Images were generally taken such that circumferential labels (parallel to the bone periosteal surface) were horizontal to the imaging axis.

2.3. Instrument settings of NanoIR2, NanoIR3 and O-PTIR experiments

NanoIR 2 AFM-IR (Anasys Instruments, California, USA) was utilized to acquire full IR spectra with an 860–1900 cm $^{-1}$ wavenumber range and 4 cm $^{-1}$ spectral resolution. For both spectroscopy and imaging applications, the instrument was operated in contact mode using a gold coated silicon cantilever (nominal radius 25 nm, force constant 0.07–0.4 N/m, resonance frequency 13 \pm 4 kHz) with an optical parametric oscillator (OPO) laser power of 2.54% (center frequency at 189 kHz with 50 kHz of frequency window and band pass filter turned on). For single wavenumber IR imaging studies, the scan rate was set at 0.1 Hz and height and deflection images were simultaneously obtained.

NanoIR 3 AFM-IR (Bruker, Santa Barbara, California, USA) was employed to collect full IR spectra with an 800 to 1884 cm $^{-1}$ wavenumber range and 2 cm $^{-1}$ spectral resolution. For both spectroscopy and imaging applications, the NanoIR 3 was operated in contact mode equipped with a gold coated silicon AFM tip (Bruker nIR2 gold-coated silicon nitride probe with a spring constant of 0.07–0.4 N/m and resonant frequency of 13 ± 4 kHz) and a tunable quantum cascade laser (QCL) power of 23.86% (center frequency at 189 kHz with 50 kHz of frequency window and band pass filter turned on). Pulse rate, duty cycles and Co-averages were 192.46 kHz, 2.5% and 128x, respectively. For single wavenumber IR imaging studies, the scan rate was set at 0.8 Hz and height, deflection, and PLL frequency images were simultaneously obtained.

O-PTIR (Photothermal Spectroscopy Corp. Santa Barbara, California, USA) spectra were acquired using an IR power of 80%, probe power of 10%, detector gain of 100 k and duty cycle of 3.06% with a QCL laser. The spectral range was 800 to 1840 $\rm cm^{-1}$ with a spectral resolution of 2 $\rm cm^{-1}$. Each spectrum collected was averaged over 10 individual spectral

acquisitions. Before taking a hyperspectral data set, an optical image of a region of interest (ROI) was obtained with 10X optical lens (a 15 mm working distance). When an actual data acquisition occurred, the system was automatically switched from the $10\times$ lens to $40\times$ high magnification lens (an 8 mm working distance). These settings were kept constant throughout the entire sample set to help ensure that changes in matrix/ mineral ratio values were related to tissue age and did not artificially result from changes in laser power. Prior to each hyperspectral data acquisition run, the sample chamber was purged with nitrogen gas to maintain ~ 0% relative humidity. A polyethylene terephthalate (PET) sample (provided by the manufacturer) with the known IR spectrum was employed to optimize the IR laser positions for 1730, 1410, 1260 and 875 cm⁻¹ with IR power of 49%, probe power of 50% and detector gain of 100 k. Peak ratios were evaluated across the full spectrum to make sure that O-PTIR operating conditions were yielding a consistent chemical signal.

2.4. Individual IR spectra collection by NanoIR 2 and NanoIR 3 and spectral processing

Matrix/mineral ratio values from IR spectra or IR ratio maps obtained by AFM-IR and O-PTIR throughout this study were determined using integrated areas representing matrix (1694–1625 cm⁻¹) (Paschalis et al., 2011) and mineral (1200-900 cm⁻¹) (Boskey and Pleshko Camacho, 2007). For both rapidly growing and adult mouse samples, AFM-IR spectra were collected using 1 μ m spatial separation in a 10 μ m ROI (Fig. 2D). The locations and lengths of these sets of spectra were determined by the previously collected fluorescence images (Fig. 2B). It is important to distinguish between the spatial resolution of NanoIR 2 and NanoIR 3 (~50 nm) and data collection step size employed. Due to the limited laser speed of the OPO laser, a data collection step size of 1 μm was selected to cover a larger region of interest across multiple tissue ages while collecting IR spectra with ~ 50 nm spatial resolution. Even though NanoIR 3 with the new QCL laser was able to collect IR spectra with an order of magnitude faster rate than NanoIR 2, for consistency, a data collection step size of 1 µm was maintained when collecting individual full IR spectra by NanoIR3. In order to obtain higher spatial resolutions spectral imaging, single wavenumber IR imaging was employed as described in Section 2.5.

All IR spectra were smoothed using a Savitzky-Golay filter (polynomial order 3 and side points 5) using Analysis Studio (Anasys Instruments, California, USA) and imported to Origin for further analysis. Origin (version Origin 2009, OriginLab Corporation, Northampton,

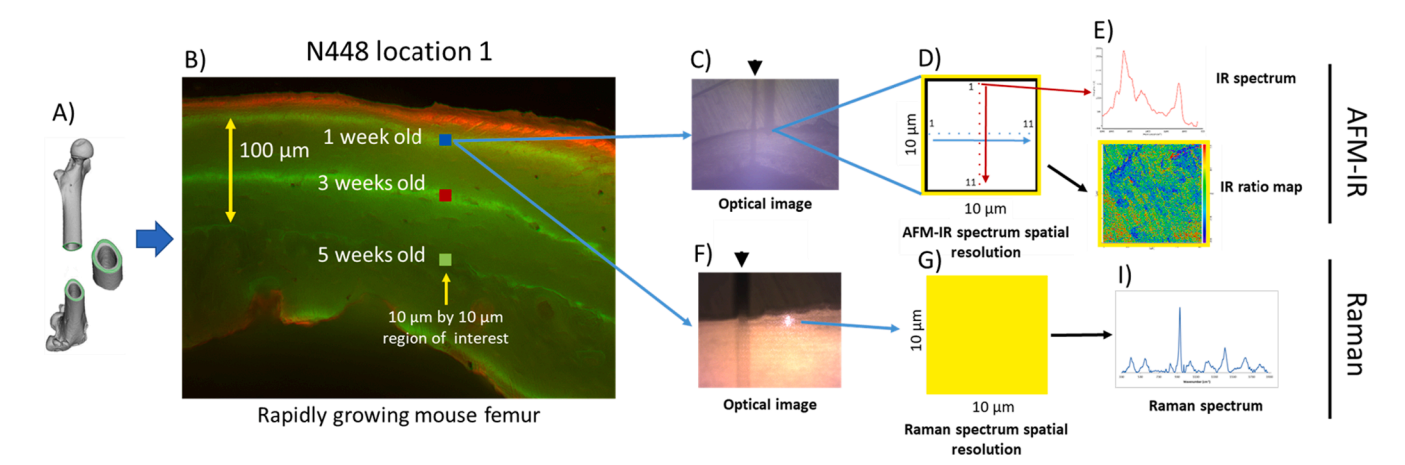


Fig. 2. Summary of AFM-IR analysis (C, D, E) and Raman analysis (F, G, I) on mouse femur. A) Femur cross-section. B) Fluorescence microscopy with imaging region of interests indicated. C) Optical image from AFM-IR microscope D) Locations of horizontal (parallel to the fluorescent lines) and vertical (perpendicular to the fluorescent lines) AFM-IR spectra obtained within 10 μ m region. E) Example of AFM-IR spectra and ratio map F) Optical image from Raman microscope. G) Raman spectral resolution (\sim 7.4 by 7.4 μ m) is comparable to the 10 \times 10 μ m region. I) Example of Raman spectrum. The colored squares indicating imaging regions in panel B are drawn to scale. The colored circles in panel D indicate the locations of IR spectra but are drawn substantially larger than scale to be visible.

Massachusetts, USA). The baseline of each spectrum was manually corrected by using "Peak Analyzer" function of Origin and the peak areas of matrix and mineral were calculated by using "Integrate" function of Origin.

2.5. Matrix/mineral IR ratio map collection by NanoIR 2 and NanoIR 3

IR ratio images were acquired using either $10\times20~\mu m$ or $10\times10~\mu m$ ROIs. Individual single wavenumber IR images collect vibration band intensity for only one preselected wavenumber; however, the single wavenumber IR imaging approach provides a significantly quicker data collection speed, thus allowing for probing a larger ROI. Wavelengths for the matrix images and mineral images were selected based on individual IR spectra obtained prior to IR ratio map acquisition. Regardless of 10×20 (33 nm by 66 nm step size) or $10\times10~\mu m$ (33 nm by 33 nm step size) dimensions, each image was obtained using 300 by 300 pixels, which was predetermined by the OPO laser pulse rate with respect to AFM scanning speed. NanoIR 3 experiments were run with the same step sizes as NanoIR 2 experiments.

To process IR ratio maps from two individual single wavenumber IR images, two height images accompanying two single wavenumber IR images were 1st order plane fit using Analysis Studio. Two single wavenumber images were subsequently ratioed by "Ratio" function under "Calculate Image" tab while the two plane fit height images were simultaneously used to correct for thermal drift. Once a ratioed IR ratio image was generated as a csv file, the ratio image could be used by other graphing software to create a figure or used to calculate domain sizes using ImageJ (version: 1.52p).

Typically, PMMA and bone exhibited different topography and could be readily distinguished by AFM maps. However, to ensure the data collection began with the first day of bone (at the bone surface), individual IR spectra were collected between PMMA and bone as shown in Figure S5.

2.6. Domain size analysis procedure

Matrix/mineral IR ratio maps were directly imported to the Fiji version of ImageJ (Schindelin et al., 2012) and thresholded by an incremental 1 numerical value of matrix/mineral ratio range and converted using the watershed function to an 8-bit binary file. The watershed image was used to calculate chemical domain sizes by using the "Analyze Particles" function. Since the data collection step size was smaller than that of the nominal AFM-IR resolution of $\sim 50~\rm nm$ the particle analyzing parameter was set to exclude particle sizes under 50 nm. Watershed images used for generating diameter sizes of chemical domains are provided in Figure S4.

2.7. Hyperspectral data collection (O-PTIR) and processing (Cytospec)

Three 5 \times 130 μm ROIs were hyperspectrally imaged using a 1 μm pixel step size (786 IR spectra collected) for four rapidly growing wild type mice femur samples using O-PTIR. A length of 130 μm , chosen to cover the Day 1 to Week 5 bone region, was determined based on fluorescence images of the bone samples.

hyperspectral data from PTIR studio thermal Spectroscopy Corp. Santa Barbara, California, USA) were converted to ASC II format and imported to Cytospec software (Berlin, Germany) for processing the hyperspectral data sets. The imported file was processed with two steps: 1) Noise reduction with 0 to 20 setting; 2) Savitzky-Golay filter with the polynomial order as 3 and side points as 11. The processed hyperspectral data was used to generate IR ratio values of matrix/mineral (peak area 1694-1626 cm⁻¹)/(peak area 1130–900 cm⁻¹). This range was used to represent mineral quantity (rather than a full 1200–900 $\mathrm{cm}^{-1}\,\mathrm{range})$ because of limited power from the QCL in the 1130-1200 cm⁻¹, resulting in a high noise level for this part of the wavelength range.

2.8. Raman spectroscopy

The x and y coordinates for the Raman spectra were determined by the fiducial mark associated with acquisition of AFM-IR spectra. The Raman microscope used for this experiment was able to move to a specific point using in-house MatlabTM code. With the same coordinate information based on the fiducial mark, AFM-IR and Raman data collection for the same tissue age regions was acquired as highlighted in Fig. 2. For each tissue age (1-week-old, 3-week-old and 5-week-old), a single Raman spectrum was acquired. The Raman microscope was equipped with a 785 nm diode laser (Innovative Photonics Solutions, Monmouth Junction, New Jersey, USA) and a 25 μm slit that can provide a spectral resolution of 4 cm⁻¹. The laser was spot-focused through a 10x0.50NA objective with a spatial resolution of $\sim 7.4 \times 7.4$ µm. The details of the instrumentation and experimental methods were previously published (Shi et al., 2018). The matrix/mineral ratio values derived from the Raman data were calculated by dividing the maximum intensity of proline and hydroxyproline bands ranging from 850 to 880 cm⁻¹ by phosphate intensity of 959 cm⁻¹ (Sinder et al., 2016). The dyes employed for fluorescent labelling in Section 2.2 (Fluorescence imaging) are not expected to affect the Raman spectra as previously demonstrated by Olejnik and co-authors (Olejnik et al., 2011) for the case of calciumbinding fluorochromes; they did not find peak shifts or overlaps with the calcein dyes.

2.9. Statistical analysis

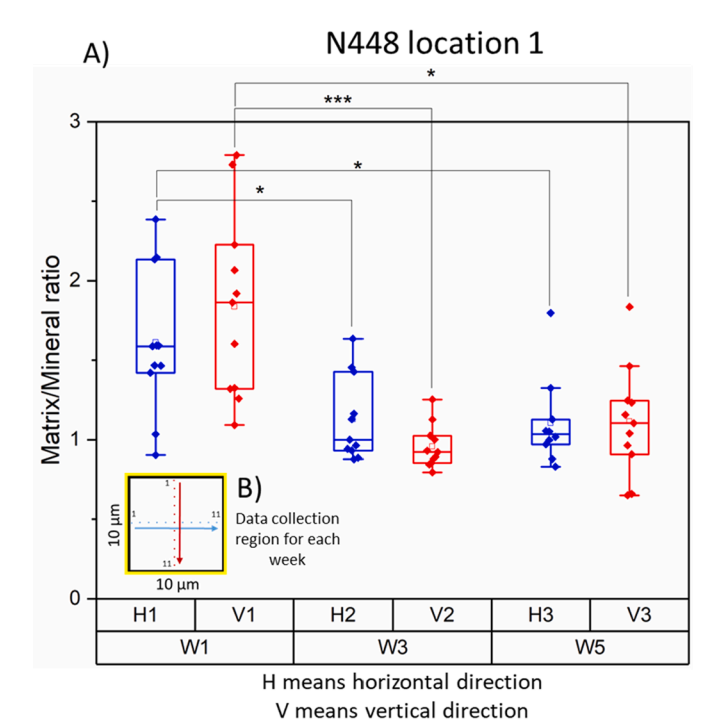
Statistical analyses of significance for mean comparisons for all data sets obtained with AFM-IR and O-PTIR in the study were determined using a non-parametric Dunn's test following Kruskal-Wallis ANOVA (OriginPro 2021, OriginLab Corporation, Northampton, MA, USA). For the matrix/mineral ratios values of different tissue ages from multiple locations and animals obtained with O-PTIR, a linear mixed effect model was employed to compare the ratio values with tissue ages as a fixed effect and animals and locations as random effects (R version: 3.6.2). The statistical model for lme4 package was constructed with 3 levels: 1) animals; 2) location; and 3) tissue age.

3. Results

A total of 9 individual wild type mouse femur samples were collected from two age groups; adult and rapidly growing juveniles. Three different characterization techniques were utilized to assess changes in matrix/mineral ratio values: 1) AFM-IR; 2) O-PTIR; and 3) Raman spectroscopy. The fluorescence image of the rapidly growing wild type mouse femur contains 4 fluorochrome labels indicating corresponding tissue age (Fig. 2B). The red line indicates 1-day-old bone. The 1st, 2nd, and 3rd green lines indicate tissue ages of 1, 3, and 5-week-old, respectively. The yellow double-headed arrow indicates the distance from week 1 to week 5 bone. Optical images of the mouse femur from the AFM-IR microscope (Fig. 2C) and Raman microscope (Fig. 2F) were used to determine comparable data collection locations for the two techniques. The black arrowheads in panels C and F indicate a cut line serving as a fiducial mark to aid in acquiring AFM-IR and Raman data over a similar ROI.

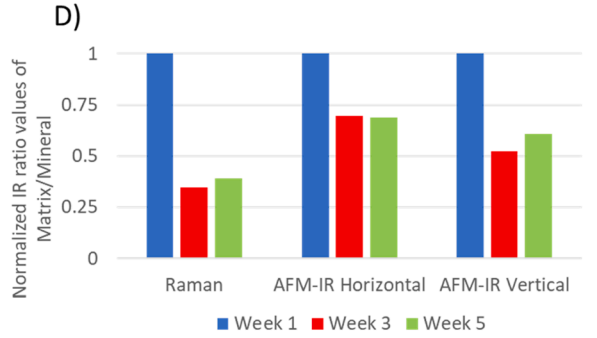
3.1. The average and extent of variation in matrix/mineral ratio values for rapidly growing wild type mouse femur decreases with tissue age

The average matrix/mineral ratio values as well as the range of ratio values obtained from AFM-IR analysis decreases as bone tissue becomes mature (Fig. 3). Panels A and C illustrate that the largest average ratio value change occurs from 1-week-old to 3-week-old tissue age as the horizontal (parallel to the circumferential fluorescent lines) matrix/mineral ratio values decrease from 1.6 to 1.1. However, the average ratio values do not significantly differ between 3-week-old and 5-week-



C)

Tissue Age	Horizontal IR ratio values average	Vertical IR ratio values average
Week 1	1.6 ± 0.4	1.8 ± 0.6
Week 3	1.1 ± 0.3	1.0 ± 0.1
Week 5	1.1 ± 0.3	1.1 ± 0.3



(Amide I/Mineral ratio: peak area of 1694-1625 cm⁻¹/ peak area of 1200-900 cm⁻¹)

Fig. 3. Matrix/mineral ratios (defined as peak area of $1694-1625~cm^{-1}$ /peak area of $1200-900~cm^{-1}$) obtained using AFM-IR for rapidly growing mice femurs collected from the 1 μ m spaced horizontal (H: blue label) and vertical (V: red label) locations for 1, 3, and 5 week old tissue age ROI as highlighted in Fig. 2B. A) Box plots of matrix/mineral ratios. Each plot contains 11 data points except Week 5H box (10 data points). B) Location of horizontal and vertical spectra collected with 1 μ m spacing in the $100~\mu m^2$ ROI. C) Average ratio values for 1, 3, and 5-week-old tissue. D) Bar graph showing normalized IR and Raman spectroscopy matrix/mineral ratio values for each corresponding tissue age. (* p < 0.05, ** p < 0.005, *** p < 0.0005). W = week, in all cases. (For interpretation of the references to color in this figure legend, the reader is referred to the web version of this article.)

old tissue. The variation in matrix/mineral ratio values found within the $10\times10~\mu m$ ROI (Fig. 3B) is the largest for 1-week-old tissue. Interestingly, the range of matrix/mineral values was similar for both the horizontal (constant tissue age) and vertical (increasing tissue age, perpendicular to the fluorescent labels) data sets within the ROI. Both the ratio range and the standard deviation decrease as tissue matures. A one-way ANOVA analysis indicates the 1-week-old matrix/mineral ratio data for the horizontal and vertical directions differs statistically from the 3-week-old and 5-week-old ratio data. However, the 3-week-old and 5-week-old IR ratio values do not statistically different from each other (p=0.99 for H2 & H3, p=0.63 for V2 & V3). In other words, within the $10\times10~\mu m$ ROI at the W1, W3, and W5 timepoints, the matrix/mineral variation for tissue that is nominally the same age (horizontal trace) does not differ significantly from tissue where the age does by several days (vertical trace).

The spatial resolution of Raman spectra acquired in this study is $\sim 7.4 \times 7.4~\mu m$ (Shi et al., 2018). Raman-derived matrix/mineral ratio values (1662 cm $^{-1}/958~cm^{-1}$) (Morris and Mandair, 2011) for the 1, 3, and 5-week-old bone regions are 0.23, 0.08, and 0.09, respectively. Fig. 3D compares normalized matrix/mineral ratio values from Raman and AFM-IR (both horizontal and vertical directions) and indicates overall agreement in matrix/mineral ratio trend for the techniques. However, AFM-IR provides an order of magnitude smaller spatial resolution as compared to the Raman instrument. Both individual IR spectra and IR ratio maps obtained by AFM-IR were collected with 1 μ m and 33 nm \times 33 nm or 33 nm \times 66 nm step sizes, respectively. Therefore, AFM-IR is able to provide the extent of matrix/mineral ratio variation (Fig. 3A) within bone regions where Raman provides a single average ratio value.

3.2. The average and extent of variation in matrix/mineral ratio values for adult wild type mouse femur decreases with tissue age

The matrix/mineral ratio values from the adult mouse femurs display a trend consistent with those from the rapidly growing mice femurs; namely, as tissue becomes mature, both the average matrix/mineral ratio values and the range of the ratio values decrease (Fig. 4). The average ratio values exhibit significant changes from 2.4 to 1.2 to 0.7 for, W1, W3, and W5 horizontal data collections, respectively, which measure the tissue at constant age. We also provide a vertical average of the data at each ROI to provide an understanding of how this data would be represented using methods achieving a $\sim 10 \, \mu m$ imaging resolution, such as the Raman data provided for comparison in this study. In this case, the average vertical matrix/mineral ratio values for W1 to W3, W3 to W5, and > W5 (older than Week 5 tissue age) do not significantly differ as one 10 µm ROI encompasses both 1-week-old to 3-week-old bone and the second ROI spans both 3-week-old bone to 5-week-oldbone. This data demonstrates how low-resolution imaging averages key age-dependent changes in matrix/mineral ratio (p = 0.16 for W1 to W3 & W3 to W5, p = 0.17 for W1 to W3 & >W5, p = 0.93 for W3 to W5 & >W5).

Unlike the rapidly growing bone case shown in Fig. 3, where a greater extent of tissue growth between weeks allowed the $10\,\mu m$ ROI to capture an accurate average matrix/mineral ratio, for the adult mouse femur highlighted in Fig. 4 the reduced inter-label distance and more spatially compact matrix/mineral changes require the enhanced resolution of the AFM-IR microscope to accurately evaluate the matrix/mineral ratio variation with age.

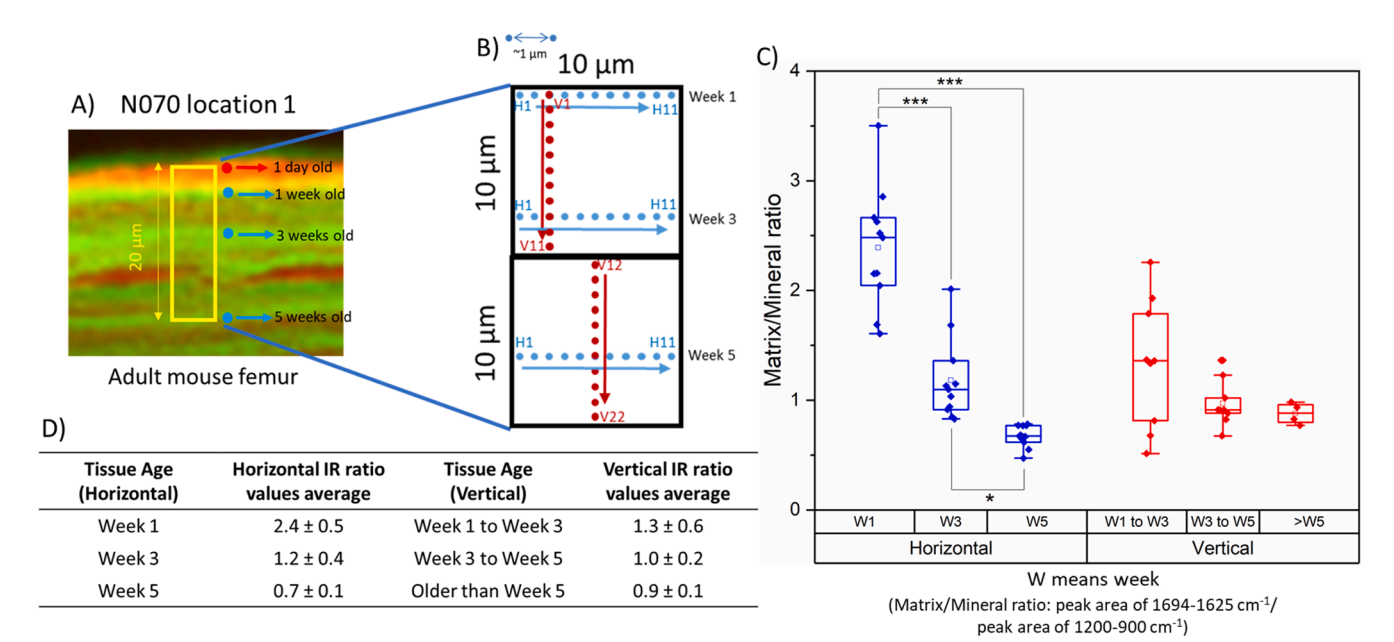


Fig. 4. Matrix/mineral ratios (defined as peak area $1694-1625 \text{ cm}^{-1}/\text{peak}$ area $1200-900 \text{ cm}^{-1}$) obtained using AFM-IR for adult mice femur. A) Fluorescence image of adult wild type mouse femur B) Location of horizontal (parallel to the fluorescent lines) and vertical (perpendicular to the fluorescent lines) spectra collected with 1 μ m spacing in $100 \ \mu\text{m}^2$ box. C) Box plots of matrix/mineral ratio for 1, 3, and 5-week-old tissue ages. Each horizontal box plot contains 11 data points while W1 to W3 and W3 to W5 vertical box plots contain 9 data points each and > W5 vertical box plot contains 4 data points. D) Average IR ratio values from horizontal and vertical directions for week 1, 3, 5 and > W5 with standard deviations. (*p < 0.05 for W3 & W5, **** p < 0.0005 for W1 &W 3 and W1 and W5, all for horizontal direction) (p = 0.16 for W1 to W3 & W3 to W5, p = 0.17 for W1 to W3 & >W5, p = 0.93 for W3 to W5 & >W5, all for vertical direction). W = week in all cases.

3.3. AFM-IR derived matrix/mineral ratio maps for adult wild type mouse femurs indicate $1-6 \mu m$ wide banding parallel to the bone surface

The IR ratio map for 1-day-old to 3-week-old tissue illustrated in Fig. 5C indicates $1-2~\mu m$ domains containing regions of greater matrix/mineral content (~3–4, green colored regions) running parallel to the tissue age domains that are indicated by fluorescent labels (Fig. 5A). These domains of greater matrix/mineral ratio values (i.e., matrix-rich tissue) are limited to tissue younger than 3 weeks of age. Histograms for the 1-day-old to 3-week-old and 3-week-old to 5-week-old tissue demonstrate the same trend (Fig. 5B). Three IR spectra (Fig. 5D), acquired from the locations noted by red circles in Fig. 5C further illustrate

this trend.

Scan direction and its interaction with surface topography can induce imaging artifacts in hybrid AFM techniques where the topography change induces undesired signal in the non-topographical channel (in this case, measurement of transient thermal expansion leading to the desired infrared absorption data). In order to check for the presence of such an artifact, we acquired data using a perpendicular scan direction (Fig. 5E). IR ratio maps 5C and 5E display a consistent set of features regardless of the scan direction. Consistent IR ratio maps, independent of AFM scan direction, are also demonstrated by additional data illustrated in Figure S2 using two 3 \times 3 μm images. We note that the Anasys NanoIR2 is designed for the scan direction highlighted in Fig. 5C and

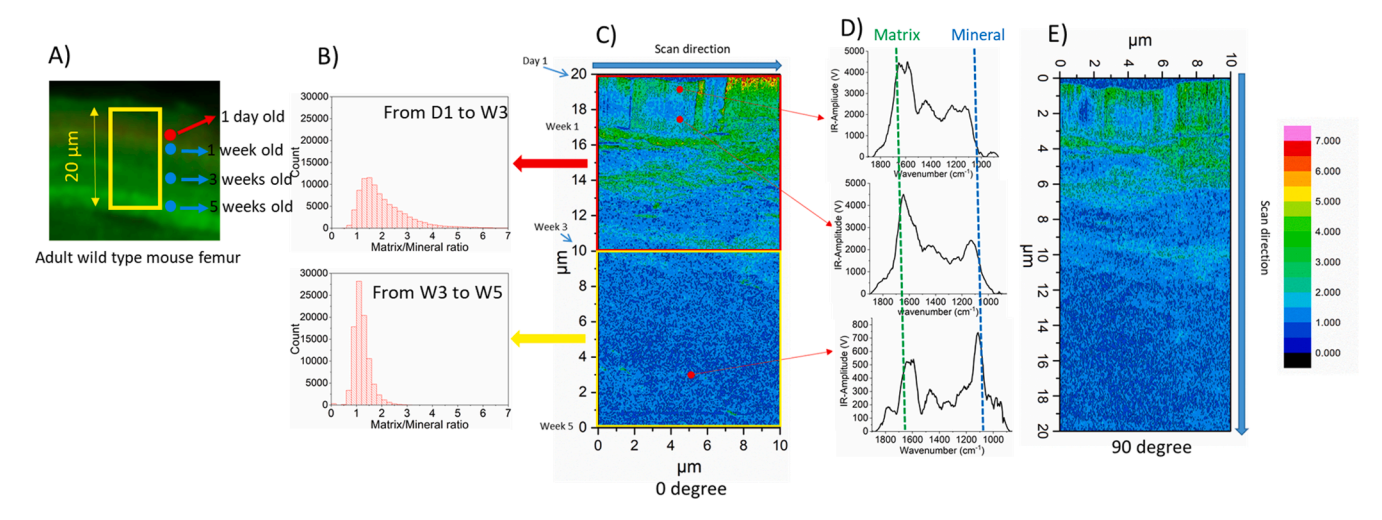


Fig. 5. Matrix/mineral ratio (defined as $1676~cm^{-1}/1080~cm^{-1}$) maps obtained using AFM-IR as a function of scan angle (0 and 90-degree) for an adult wild type mouse femur (N030, location 1). A) Fluorescence microscope image. The vertical yellow box indicates the area where IR data was collected. B) Histograms of each $10 \times 10~\mu m$ IR ratio map from panel C. C) IR ratio map from 1-day-old to 5-week-old measured using a 0-degree scan (standard operating condition) D) Individual IR spectra obtained from red circled regions on the IR ratio map. E) IR ratio measured using a 90-degree scan angle over the same region. (For interpretation of the references to color in this figure legend, the reader is referred to the web version of this article.)

that normal acquisition of data using a perpendicular scan direction (Fig. 5E) is not a factory recommended operation procedure. The IR ratio map and histograms from sample N046 acquired using a Bruker NanoIR 3 (a newer version of AFM-IR instrument) are shown in Figure S1 and are also consistent with trends illustrated in Fig. 5.

In Fig. 6, matrix/mineral images are provided for three adult mice femurs (two locations for each femur). A summary set of boxplots containing all matrix/mineral ratio values from the three samples (N030, N041 and N045) highlights the general relation of a matrix/mineral map to the horizontal and vertical data acquisition regions (Fig. 6G). There are two significant, quantitative results apparent from the summary box plots as the tissue becomes more mature: 1) the average matrix/mineral ratio values decrease. The largest change is observed after the 1-weekold tissue age; 2) the range of matrix/mineral ratio values decreases. In addition, the IR ratio maps highlight location-to-location and animalto-animal variation. For example, panel A shows a different mineralization level for 3 to 5-week-old tissue age as compared to panel B (location-to-location difference) and from panel F (animal-to-animal difference). A common feature to all ratio maps in Fig. 6 is the horizontal matrix/mineral alternating banding pattern, which exhibits a varying ~ 1 to 6 µm width range. Panels B, C and E show a relatively smaller banding size of ~ 1 µm while panels A, B, E and F exhibit a larger banding size of ~ 3 to 6 μm . This type of alternating mineral-to-matrix ratio pattern was previously observed by Imbert et al. with AFM-IR on chemically dehydrated cancellous bone samples. They reported the alternating pattern exhibited periodicities of 2–8 µm based on their line scan IR spectra and IR maps of the mineral-to-matrix ratio (Imbert et al., 2018).

3.4. AFM-IR derived matrix/mineral ratio maps from adult wild type mouse femurs indicate ~ 50 to 700 nm range of domain sizes

The matrix/mineral maps show a variety of matrix/mineral regions including the matrix-rich horizontal banding highlighted in the D1 to W3 region and mineral-rich speckling noted in the W3 to W5 regions

(Fig. 7). These size of the domains as a function of matrix/mineral ratio is summarized as a series of boxplots in Fig. 7C, which shows a range from ~ 50 to 700 nm. The domain sizes for matrix/mineral ratio values <5 tend to be larger, ranging from ~ 50 to 500 nm, with the key exception of the matrix/mineral ratio range from 1 to 2 that exhibits the largest average domain size as well as range up to ~ 700 nm diameter. The domain sizes calculated for matrix/mineral ratio values > 5 tend to be smaller, nominally ranging from ~ 50 to 200 nm. Examples of each measured individual domain with different thresholds can be found in Figure S4.

3.5. O-PTIR data from rapidly growing wild type mouse femurs exhibits larger domains ranging from \sim 20 to 40 μm with a more uniform mineralization level and smaller domains ranging from \sim 1 to 5 μm with a lower mineralization level

Fig. 8B illustrates an O-PTIR matrix/mineral map derived from a hyperspectral data set acquired from a rapidly growing mouse femur sample. The O-PTIR hyperspectral data set consists of a two-dimensional chemical map where each data point is a full IR spectrum rather than a ratio value from two single wavenumber IR maps as was obtained for AFM-IR data. The data collection step size is $1\times 1~\mu m$, generating a minimum of 786 full IR spectra for each ROI. With this type of data set, it is possible to measure an ROI fully encompassing the 1-day-old to 5-week-old bone regions.

The matrix/mineral ratio maps from N448 and N383 illustrated in Fig. 9A show higher ratio values from the younger bone regions while the IR ratio maps from 367 and 368 do not, except for the location 1 of sample 367. The ratio maps from the four samples display two distinctive matrix/mineral ratio patterns: 1) vertically long regions ranging from \sim 20 to 40 μm where a more uniform level of matrix/mineral ratio values (either high such as N448 and N383 or low such as 367 and 368) is observed; 2) smaller domains ranging from \sim 1 to 5 μm where high matrix/mineral ratio values were observed across all four samples. These longer uniform regions and smaller pockets of a different

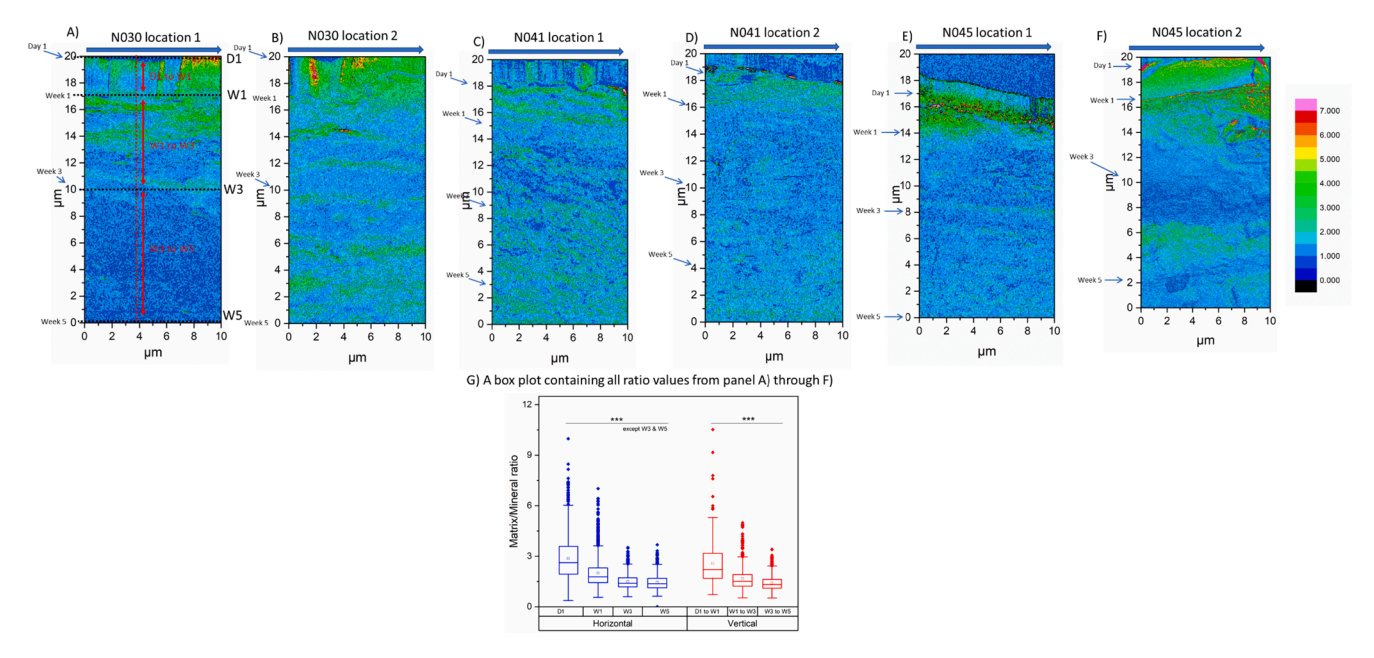


Fig. 6. A-F) Individual IR ratio maps indicating horizontal and vertical cross-section and G) a box plot combining all matrix/mineral ratio values of three adult mice femurs (N030, N041 and N045) as a function of sample and tissue age. The ratio values for N030 and N041 are based on matrix (1676 cm^{-1})/mineral (1080 cm^{-1}). For N045, matrix (1664 cm^{-1})/mineral (1108 cm^{-1}). Matrix values were selected based on the average maximum peak position. Individual box plots for panels A) through F) are provided in Figure S3. The summary box plot containing all ratio values shows that as bone samples become mature, both the mean IR matrix/mineral ratio values as well as of the range of observed matrix/mineral ratio values decreases. (*p < 0.05, **p < 0.005, ***p < 0.0005). D = day, W = week in all cases. However, the individual IR ratio maps demonstrate different chemical compositional patterns for each sample and location, indicating a heterogeneous nature of bone chemical composition.

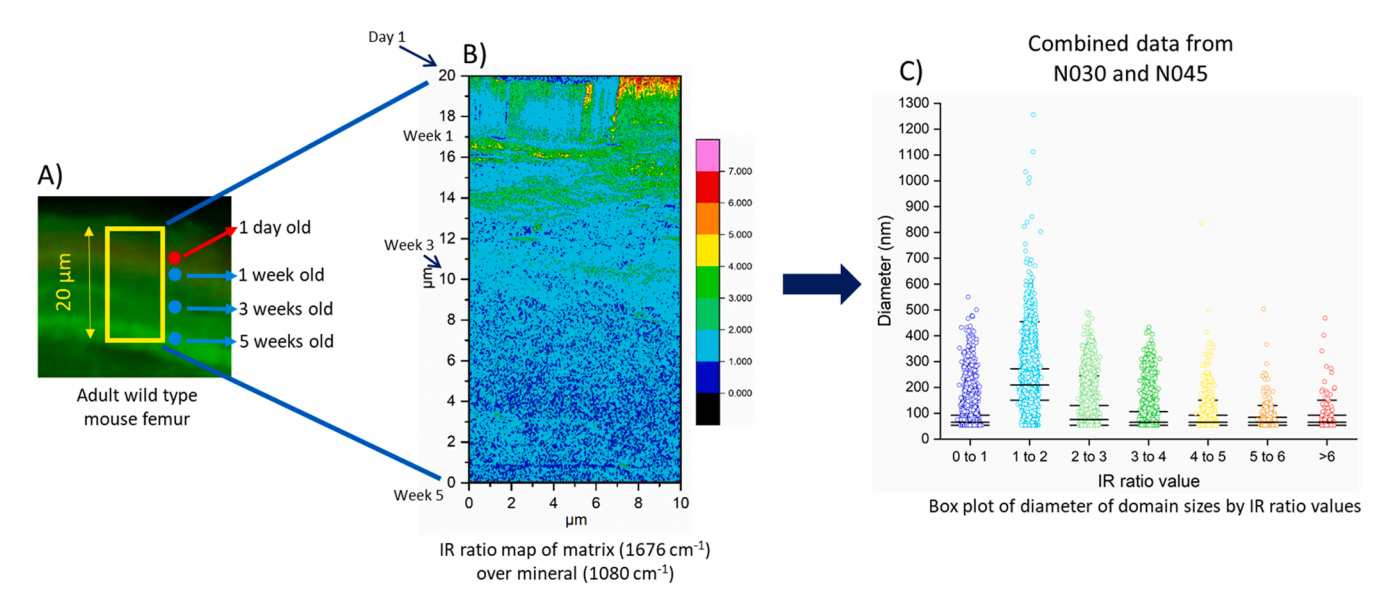


Fig. 7. Quantification of domain sizes for a given range of matrix/mineral ratios in adult mice femurs. A) Exemplar fluorescence microscope image indicating location of IR map B) Exemplar IR ratio map C) an I-shaped box plot summarizing domain size as a function of all matrix/mineral ratio values obtained from two samples (N030 and N045). The color of each I-shaped box plot matches the color scale of the IR ratio map. There are four black lines for each I-shaped box plot. Two outer lines indicate whisker ranges. Two inter lines indicate box ranges from 25 to 75%.

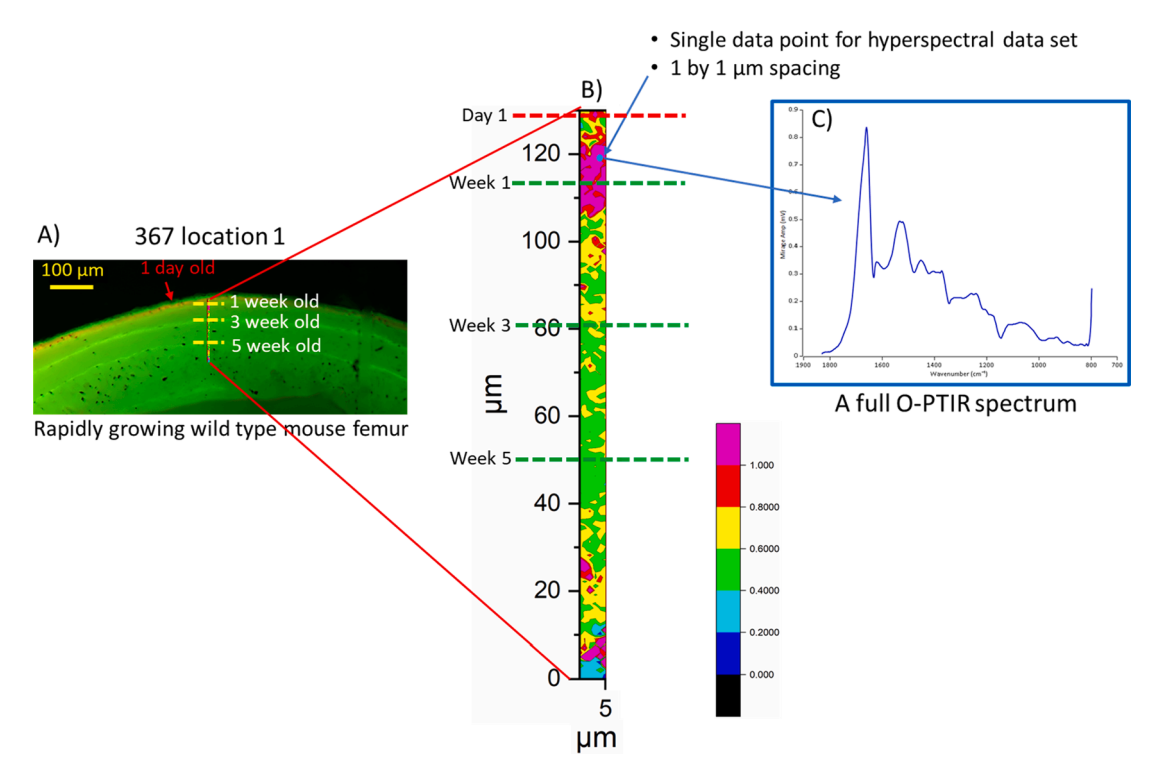
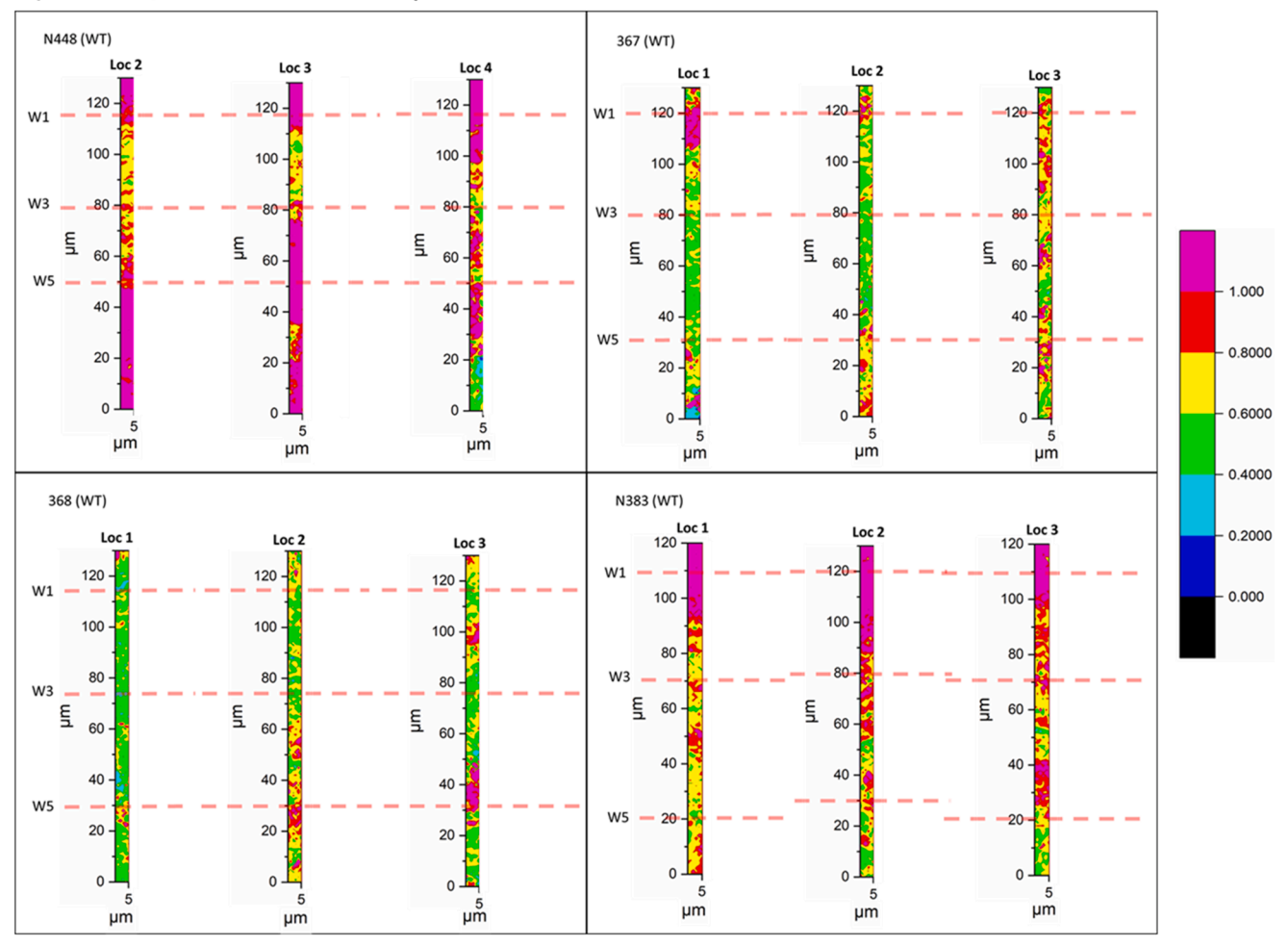


Fig. 8. Matrix/mineral ratio map (peak area 1694 to $1626 \, \mathrm{cm}^{-1}$)/(peak area $1130 \, \mathrm{to} \, 900 \, \mathrm{cm}^{-1}$) obtained from hyperspectral optical photothermal infrared (OPTIR) spectroscopy data set for a rapidly growing juvenile mouse femur. A) Exemplar fluorescence microscope image indicating location of four different tissue ages. B) Exemplar IR matrix/mineral ratio map. The blue dot represents the approximate step size of IR data collection ($1 \times 1 \, \mu m$). C) Exemplar O-PTIR spectrum taken from location indicated by blue dot obtained from the hyperspectral O-PTIR data set. (For interpretation of the references to color in this figure legend, the reader is referred to the web version of this article.)

mineralization level from O-PTIR are similar to the two IR patterns of the larger banding pattern with ~ 1 to 6 μm width and smaller domain sizes ranging from ~ 50 to 700 nm found from AFM-IR. These highly localized bone compositional differences identified in the IR ratio maps yield an average set of ratio values when pooled together (Fig. 9B and C) that is consistent with the previously described trends found from AFM-IR and Raman spectroscopy.

A) Matrix/Mineral ratio maps from individual location



B) A box plot combining all ratio values C) A box plot combining all ratio values (full y-axis range) (y-axis range less than 4)

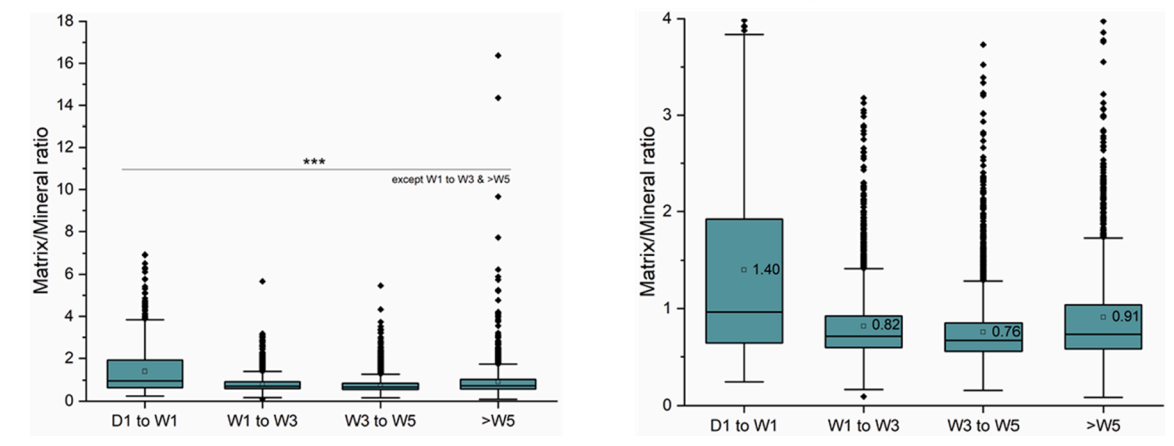


Fig. 9. A) Matrix/mineral ratio (peak area 1694 to 1626 cm⁻¹)/(peak area 1130 to 900 cm⁻¹) maps for rapidly growing juvenile mice femurs. B) A summary box plot containing all matrix/mineral ratio values from four samples (N448, 367, 368 and N383) with a full y-axis range, displaying all outliers. C) A summary box plot containing all matrix/mineral ratio values from four samples with the range of y-axis limited to 4.

4. Discussion

4.1. Matrix/mineral ratio trends obtained from AFM-IR and O-PTIR are consistent with conventional IR and Raman microscopy spectroscopy data; in addition, they provide novel information on micron-scale matrix/mineral banding and nano- to micron scale domain structure

The AFM-IR and O-PTIR, and Raman data sets in this study show a decreasing matrix/mineral ratio, consistent with a greater degree of mineralization, with increasing tissue age. This overall trend is well documented in literature (Boskey and Pleshko Camacho, 2007; Roschger and Misof, 2020; Turunen et al., 2011). Imbert et al. employed AFM-IR (NanoIR 2) to evaluate the composition of chemically fixed and dehydrated vertebral biopsies from ovariectomized (OVX) sheep. They found increasing mineral to matrix ratio values as a function of trabecular location, consistent with increasing mineralization from younger bone at the trabecular surface to more mature bone inside of the trabecula (Imbert et al., 2018).

Sinder et al. performed Raman spectroscopy on the same set of the rapidly growing juvenile and adult mice femur samples employed for AFM-IR and O-PTIR in this study (Sinder et al., 2016). They chose mineral/matrix (958 cm⁻¹/max(840 cm⁻¹–900 cm⁻¹)) ratio to estimate relative changes in matrix (proline intensity) and mineral. For the rapidly growing mouse femur samples, the mineral/matrix ratio values increased and plateaued at 3-week-old tissue age. On the other hand, the mineral/matrix ratio values from the adult samples kept increasing over time (Sinder et al., 2016).

The overall trends of the present AFM-IR data and Raman data (matrix/mineral; 1662 cm⁻¹/958 cm⁻¹) from the rapidly growing sample mouse samples agree with the findings by Sinder et al. AFM-IR characterization shows the average matrix/mineral ratio values from 3-week-old and 5-week-old are over 30% reduced, compared to the average ratio values from 1-week-old (Fig. 3). However, the average ratio values remain consistent between 3-week-old and 5-week-old tissue. In addition, the values measured using Raman spectroscopy decrease from 0.23 (1-week-old) to 0.1 (3-week-old), and 0.1 (5-weekold). The AFM-IR data from the adult mouse sample in Fig. 4 is also consistent with the ratio trend reported by Sinder et al. The average matrix/mineral ratio values decrease in a statistically significant fashion from 1-week-old through 5-week-old tissue (Fig. 4). The matrix/mineral ratio values from both Figs. 3 and 4 are calculated from individual IR spectra obtained with 1 µm spacing in a 10 µm ROI, which is similar to how the ratio values were obtained by Sinder et al., which utilized a ~ 3 µm spacing parallel to the constant age fluorescence marker (Sinder et al., 2016). Additionally, the consistent mineralization trend between AFM-IR/O-PTIR and Raman agrees with the findings by Turunen et al. (Turunen et al., 2011) who compared the aging effects on bone mineralization between FTIR and Raman spectroscopy techniques and found a linear correlation of mineral/matrix ratio values. However, they discovered that a higher correlation between bone mineral density (BMD) by micro-CT and Raman (p < 0.01) as compared to that between BMD and FTIR (p < 0.05), suggesting that Raman might be more sensitive to mineral content in bone. In this study, we do not directly compare AFM-IR/O-PTIR ratio values to these of Raman. Rather, we compare the overall mineralization trend between AFM-IR/O-PTIR and Raman. Therefore, this direct comparison to Raman microscopy using the same sample set provides a validation of the AFM-IR and O-PTIR methods for evaluating matrix/mineral ratio in bone. In addition to obtaining data consistent with overall matrix/mineral trends with tissue age, the photothermal methods can also characterize spatial distribution of different bone mineralization levels in a several-times finer resolution than the conventional spectroscopic methods.

4.2. Domain sizes obtained from IR matrix/mineral ratio maps are comparable to the domain sizes in nanoscale mechanical maps obtained by AFM-based nanoindentation

The nominal domain size range of ~ 100 to 500 nm derived from mechanical maps for adult ovine cortical bone(Tai et al., 2007) is consistent with the domain size obtained from AFM-IR matrix/mineral ratio maps (Fig. 7). The mineral component in bone is associated with bone stiffness (Fratzl et al., 2004) and the matrix/mineral ratio values indicate overall mineralization level in bone. Therefore, it is plausible that the variation in the extent of nanoscale mineralization in bone identified by the matrix/mineral ratio maps is a contributing factor in the measured nanoscale mechanical heterogeneity. Recently, Langelier et al. employed atomic probe tomography coupled with TEM to study chemical heterogeneity at the nanoscale in human bone samples (Langelier et al., 2017). They discovered nanoscale variation in the concentration of Ca, P, and Na (mineral components) in three-dimensions on the 10-20 nm length-scale. Mineral gradient maps showed plate-like crystals displaying alternating Ca rich and deficient regions whose width is 50-70 nm.

The AFM-IR matrix/mineral maps, atomic probe tomography maps, and AFM-indentation maps are all consistent with nanoscale chemical heterogeneity in bone. To further probe these relations, the relationship between matrix/mineral ratio maps and phase-locked loop (PLL) frequency maps was explored (Figure S6); however, a relationship was not observed between the matrix/mineral map and the PLL frequency map. This may result from a substantial difference in sampling depth between the two methods. The IR laser is known to have the depth of penetration around ~ 1 to 3 μm , leading to a depth of sampling of $\gg 50$ nm, whereas the PLL frequency response is likely a more surface sensitive technique probing stiffness of just a few nanometers or at most a single fibril.

4.3. AFM-IR and O-PTIR reveal highly localized matrix/mineral domains in bone

Overall, the summary box plots from Figs. 6G and 9C display the same decreasing matrix/mineral ratio trend observed by Sinder et al. (Sinder et al., 2016) However, the matrix/mineral IR ratio maps in Figs. 6 and 9 reveal the spatially heterogenous nature of the matrix/ mineral ratio values across the tissue regions, which the box plots alone do not capture. In bone, material heterogeneity, including chemical heterogeneity, is a putative contributor to bone toughening and chemical variation in bone under a submicron length scale is not well understood (Lloyd et al., 2015). By employing fluorescence computed tomography and diffraction scattering computed tomography, Wittig et al. (Wittig et al., 2019) studied mineral properties in bone with a submicrometer resolution. The studies indicate that the mineral component in osteonal bone exhibits varying crystal composition, disorder, and crystalline size, suggesting that the mineralization process in bone varies depending on local microenvironments. Additionally, Roschger et al. found with scanning synchrotron X-ray scattering that modelling and remodelling bone regions contain mineral particles with different thickness values, also suggesting a distinctively different localized mineralization process (Roschger et al., 2020). This localized mineral difference is consistent with the chemical variation of matrix/mineral IR ratio values identified by AFM-IR and O-PTIR.

The matrix/mineral ratio maps from AFM-IR and O-PTIR display two distinctive patterns: 1) a larger alternating banding pattern running parallel to the bone surface (AFM-IR: $\sim\!1$ to 6 μm and O-PTIR: $\sim\!20$ to 40 μm); 2) smaller and more pocketed domain sizes (AFM-IR: $\sim\!50$ to 700 nm and O-PTIR: $\sim\!1$ to 5 μm). To deconvolute whether the mineral or matrix component contributes to the mineral-to-matrix ratio, Imbert et al. obtained mineral intensity, matrix intensity, and mineral-to-matrix ratio maps between untreated and demineralized bone samples.(Imbert et al., 2018) Their images show both matrix intensity and mineral-to-matrix maps from both untreated and demineralized samples

consistently display an alternating banding pattern. However, the mineral intensity map from the demineralized sample exhibits no signal. Therefore, their data suggest that spatially varying collagen density contributes to the IR ratio banding pattern.

We note a number of limitations of this study. First, since both AFM-IR and O-PTIR measure an IR signal based on the amount of thermal expansion induced by IR light absorbed by bone, depending on an extent of mineralization (i.e., a higher level of mineralization may be less sensitive to thermal expansion), the volume of analysis may change across a given bone tissue. This limitation stands in contrast to conventional FTIR studies where an absorption measurement is typically performed on a uniformly thick, albeit dehydrated, section of tissue. Second, we collected and analyzed a general mineralization level across different tissue ages. We did not measure the chemical makeup of the crystallites (e.g., lattice substitution or a level of crystallinity) which is known to vary between different tissue ages.

5. Conclusion

This study combines AFM-IR, O-PTIR, and Raman spectroscopy to characterize how matrix/mineral ratio values change as a function of bone tissue age. AFM-IR and O-PTIR are shown to produce comparable matrix/mineral ratio values to conventional FTIR and Raman spectroscopy techniques, while also providing more detailed chemical and microstructural information. In particular, there exists a matrix/mineral domain size range of ~ 50 to 700 nm and a sharp matrix/mineral transition within the length scale of 100-200 nm determined by AFM-IR. The size scale of these two features is significantly lower than the spatial resolution of FTIR and Raman spectroscopy. This study provides complementary spectroscopic characterization to the previously reported mechanical domains measured using nanoidentation. This study also indicates that the spacing of bone layers, and the associated matrix/ mineral variation, can occur in just a few microns leading to a spatially incomplete, average assessment of matrix/mineral ratios when average ROIs of 7-10 μm, as have often been employed in Raman and FTIR studies, are used as the evaluative methods. In particular, these large average ROIs fail to capture nano- to micron scale matrix/mineral banding and other spatial domains that reflect the size scale of key bone components. Similarly, the matrix/mineral ratio maps from O-PTIR demonstrate vertically long regions of \sim 20 to 40 μm where a fairly uniform level of the mineralization (either high or low) is observed and ~ 1 to 5 µm smaller domain regions where lower mineralization is observed. Both AFM-IR and O-PTIR demonstrate the presence of greater ranges of matrix/mineral ratio variation in younger tissue as compared to older tissue, which is consistent with the formation of an initial collagen matrix that is gradually and inhomogeneously filled with mineral nanocrystals.

CRediT authorship contribution statement

Taeyong Ahn: Conceptualization, Formal analysis, Investigation, Data curation, Visualization. Max Jueckstock: Investigation. Gurjit S. Mandair: Formal analysis, Investigation. James Henderson: Formal analysis. Benjamin P. Sinder: Resources. Kenneth M. Kozloff: Conceptualization, Supervision. Mark M. Banaszak Holl: Conceptualization, Supervision.

Declaration of Competing Interest

The authors declare that they have no known competing financial interests or personal relationships that could have appeared to influence the work reported in this paper.

Acknowledgments

The authors would like to thank the National Science Foundation

(NSF1634680), the National Institute of Arthritis and Musculoskeletal and Skin Diseases for the Michigan Integrative Musculoskeletal Health Core Center (P30 AR069620), and Monash University for support of this work.

Appendix A. Supplementary material

Supplementary data to this article can be found online at https://doi.org/10.1016/j.jsb.2022.107878.

References

- Bakir, G., Girouard, B.E., Wiens, R., Mastel, S., Dillon, E., Kansiz, M., Gough, K.M., 2020.
 Orientation Matters: Polarization dependent IR spectroscopy of collagen from intact tendon down to the single fibril level. Molecules 25, 4295.
- Boskey, A., Pleshko Camacho, N., 2007. FT-IR imaging of native and tissue-engineered bone and cartilage. Biomaterials 28, 2465–2478.
- Chen, J., Kim, J., Shao, W., Schlecht, S.H., Baek, S.Y., Jones, A.K., Ahn, T., Ashton-Miller, J.A., Banaszak Holl, M.M., Wojtys, E.M., 2019. An Anterior Cruciate Ligament Failure Mechanism. Am. J. Sports Med. 47, 2067–2076.
- Dazzi, A., Prater, C.B., 2017. AFM-IR: Technology and applications in nanoscale infrared spectroscopy and chemical imaging. Chem. Rev. 117, 5146–5173.
- Dazzi, A., Prater, C.B., Hu, Q., Chase, D.B., Rabolt, J.F., Marcott, C., 2012. AFM-IR: Combining atomic force microscopy and infrared spectroscopy for nanoscale chemical characterization. Appl. Spectrosc. 66, 1365–1384.
- De Carmejane, O., Morris, M.D., Davis, M.K., Stixrude, L., Tecklenburg, M., Rajachar, R. M., Kohn, D.H., 2005. Bone chemical structure response to mechanical stress studied by high pressure Raman spectroscopy. Calcif. Tissue Int. 76, 207–213.
- Fratzl, P., Gupta, H.S., Paschalis, E.P., Roschger, P., 2004. Structure and mechanical quality of the collagen-mineral nano-composite in bone. J. Mater. Chem. 14, 2115–2123.
- Gamsjaeger, S., Masic, A., Roschger, P., Kazanci, M., Dunlop, J.W.C., Klaushofer, K., Paschalis, E.P., Fratzl, P., 2010. Cortical bone composition and orientation as a function of animal and tissue age in mice by Raman spectroscopy. Bone 47, 392–399.
- Gong, B., Oest, M.E., Mann, K.A., Damron, T.A., Morris, M.D., 2013. Raman spectroscopy demonstrates prolonged alteration of bone chemical composition following extremity localized irradiation. Bone 57, 252–258.
- Gourion-Arsiquaud, S., Marcott, C., Hu, Q., Boskey, A.L., 2014. Studying Variations in Bone Composition at Nano-Scale Resolution: A Preliminary Report. Calcif. Tissue Int. 95, 413–418.
- Huang, L., Zhang, X., Shao, J., Zhou, Z., Chen, Y., Hu, X., 2020. Nanoscale chemical and mechanical heterogeneity of human dentin characterized by AFM-IR and bimodal AFM. J. Adv. Res. 22, 163–171.
- Imbert, L., Gourion-Arsiquaud, S., Villarreal-Ramirez, E., Spevak, L., Taleb, H., van der Meulen, M.C.H., Mendelsohn, R., Boskey, A.L., 2018. Dynamic structure and composition of bone investigated by nanoscale infrared spectroscopy. PLoS One 13, 1–15.
- Jones, R.R., Hooper, D.C., Zhang, L., Wolverson, D., Valev, V.K., 2019. Raman Techniques: Fundamentals and Frontiers. Nanoscale Res. Lett. 14, 231.
- Kansiz, M., Prater, C., Dillon, E., Lo, M., Anderson, J., Marcott, C., Demissie, A., Chen, Y., Kunkel, G., 2020. Optical Photothermal Infrared Microspectroscopy with Simultaneous Raman A New Non-Contact Failure Analysis Technique for Identification of <10 μm Organic Contamination in the Hard Drive and other Electronics Industries. Micros. Today 28, 26–36.</p>
- Khanal, D., Zhang, J., Ke, W.R., Banaszak Holl, M.M., Chan, H.K., 2020. Bulk to Nanometer-Scale Infrared Spectroscopy of Pharmaceutical Dry Powder Aerosols. Anal. Chem. 92, 8323–8332.
- Klementieva, O., Sandt, C., Martinsson, I., Kansiz, M., Gouras, G.K., Borondics, F., 2020. Super-Resolution Infrared Imaging of Polymorphic Amyloid Aggregates Directly in Neurons. Adv. Sci. 7, 1–9.
- Langelier, B., Wang, X., Grandfield, K., 2017. Atomic scale chemical tomography of human bone. Sci. Rep. 7, 1–9.
- Lloyd, A.A., Wang, Z.X., Donnelly, E., 2015. Multiscale Contribution of Bone Tissue Material Property Heterogeneity to Trabecular Bone Mechanical Behavior. J. Biomech. Eng. 137, 1–8.
- Lopes, C. de C.A., Limirio, P.H.J.O., Novais, V.R., Dechichi, P., 2018. Fourier transform infrared spectroscopy (FTIR) application chemical characterization of enamel, dentin and bone. Appl. Spectrosc. Rev. 53, 747–769.
- Miller, L.M., Smith, R.J., 2005. Synchrotrons versus globars, point-detectors versus focal plane arrays: Selecting the best source and detector for specific infrared microspectroscopy and imaging applications. Vib. Spectrosc. 38, 237–240.
- Morris, M.D., Mandair, G.S., 2011. Raman assessment of bone quality. Clin. Orthop. Relat. Res. 469, 2160–2169.
- Nyman, J.S., Makowski, A.J., Patil, C.A., Masui, T.P., O'Quinn, E.C., Bi, X., Guelcher, S. A., Nicollela, D.P., Mahadevan-Jansen, A., 2011. Measuring differences in compositional properties of bone tissue by confocal raman spectroscopy. Calcif. Tissue Int. 89, 111–122.
- Olejnik, C., Falgayrac, G., During, A., Penel, G., 2011. Compatibility of fluorochrome labeling protocol with Raman spectroscopy to study bone formation. Bull. Group. Int. Rech. Sci. Stomatol. Odontol. 50, 34–36.

- Olson, N.E., Xiao, Y., Lei, Z., Ault, A.P., 2020. Simultaneous Optical Photothermal Infrared (O-PTIR) and Raman Spectroscopy of Submicrometer Atmospheric Particles. Anal. Chem. 92, 9932–9939.
- Paschalis, E.P., Mendelsohn, R., Boskey, A.L., 2011. Infrared assessment of bone quality: A review. Clin. Orthop. Relat. Res. 469, 2170–2178.
- Roschger, A., Wagermaier, W., Gamsjaeger, S., Hassler, N., Schmidt, I., Blouin, S., Berzlanovich, A., Gruber, G.M., Weinkamer, R., Roschger, P., Paschalis, E.P., Klaushofer, K., Fratzl, P., 2020. Newly formed and remodeled human bone exhibits differences in the mineralization process. Acta Biomater. 104, 221–230.
- Roschger, P., Misof, B.M., 2020. Basic Aspects of Bone Mineralization. Springer Nat. 89–113.
- Schindelin, J., Arganda-Carreras, I., Frise, E., Kaynig, V., Longair, M., Pietzsch, T., Preibisch, S., Rueden, C., Saalfeld, S., Schmid, B., Tinevez, J.-Y., White, D.J., Hartenstein, V., Eliceiri, K., Tomancak, P., Cardona, A., 2012. Fiji: an open-source platform for biological-image analysis. Nat. Meth. 9 (7), 676–682.
- Sereda, G., VanLaecken, A., Turner, J.A., 2019. Monitoring demineralization and remineralization of human dentin by characterization of its structure with resonance-enhanced AFM-IR chemical mapping, nanoindentation, and SEM. Dent. Mater. 35, 617–626.

- Shi, C., Mandair, G.S., Zhang, H., Vanrenterghem, G.G., Ridella, R., Takahashi, A., Zhang, Y., Kohn, D.H., Morris, M.D., Mishina, Y., Sun, H., 2018. Bone morphogenetic protein signaling through ACVR1 and BMPR1A negatively regulates bone mass along with alterations in bone composition. J. Struct. Biol. 201, 237–246.
- Sinder, B.P., Lloyd, W.R., Salemi, J.D., Marini, J.C., Caird, M.S., Morris, M.D., Kozloff, K. M., 2016. Effect of anti-sclerostin therapy and osteogenesis imperfecta on tissue-level properties in growing and adult mice while controlling for tissue age. Bone 84, 222–229.
- Tai, K., Dao, M., Suresh, S., Palazoglu, A., Ortiz, C., 2007. Nanoscale heterogeneity promotes energy dissipation in bone. Nat. Mater. 6, 454–462.
- Taylor, E.A., Donnelly, E., 2020. Raman and Fourier transform infrared imaging for characterization of bone material properties. Bone 139, 115490.
- Turunen, M.J., Saarakkala, S., Rieppo, L., Helminen, H.J., Jurvelin, J.S., Isaksson, H., 2011. Comparison between infrared and raman spectroscopic analysis of maturing rabbit cortical bone. Appl. Spectrosc. 65, 595–603.
- Wittig, N.K., Palle, J., Østergaard, M., Frølich, S., Birkbak, M.E., Spiers, K.M., Garrevoet, J., Birkedal, H., 2019. Bone Biomineral Properties Vary across Human Osteonal Bone. ACS Nano 13, 12949–12956.
- Yao, H., Dao, M., Carnelli, D., Tai, K., Ortiz, C., 2011. Size-dependent heterogeneity benefits the mechanical performance of bone. J. Mech. Phys. Solids 59, 64–74.